Applied Catalysis B: Environmental 179 (2015) 333–343

Contents lists available at ScienceDirect

Applied Catalysis B: Environmental

journal homepage: www.elsevier.com/locate/apcatb

Enhanced photocatalytic properties of core@shell SiO_2@TiO_2 nanoparticles

Sajjad Ullah[a,b], Elias P. Ferreira-Neto[a], André A. Pasa[c], Carlos C.J. Alcântara[c], José J.S. Acuña[d], Sara A. Bilmes[e], Maria L. Martínez Ricci[e], Richard Landers[f], Taina Zampieri Fermino[a], Ubirajara P. Rodrigues-Filho[a,*]

[a] Grupo de Química de Materiais Híbridos e Inorgânicos, Instituto de Química de São Carlos, Universidade de São Paulo, São Carlos, São Paulo, PO Box 780, 13564-970, Brazil
[b] Institute of Chemical Sciences, University of Peshawar, Peshawar 25120 KP, Pakistan
[c] Laboratório de Filmes Finos e Superfícies, Departamento da Física, Universidade Federal de Santa Catarina, PO Box 476, 88040-900 Florianópolis, SC, Brazil
[d] Centro de Ciências Naturais e Humanas, Universidade Federal do ABC, Sao Paulo, Brazil
[e] Instituto de Química Física de los Materiales, Medio Ambiente y Energía – INQUIMAE, DQIAQF, Facultad Ciencias Exactas y Naturales, Ciudad Universitaria, Universidad de Buenos Aires, Buenos Aires, Pabellón 2, C1428EHA, Argentina
[f] Instituto de Física Gleb Wataghin (IFGW), Universidade Estadual de Campinas (UNICAMP), Campinas, SP, Brazil

ARTICLE INFO

Article history:
Received 8 December 2014
Received in revised form 2 May 2015
Accepted 15 May 2015
Available online 19 May 2015

Keywords:
SiO_2@TiO_2
Core@shell
Optical properties
Rayleigh scattering
Quantum size effect
Photocatalysis

ABSTRACT

SiO_2@TiO_2 core@shell nanoparticles (CSNs) have recently attracted great attention due to their unique and tunable optical and photocatalytic properties and higher dispersion of the supported TiO_2. Thus, development of facile, reproducible and effective methods for the synthesis of SiO_2@TiO_2 CSNs and a fundamental understanding of their improved properties, derived from combination of different core and shell materials, is of great importance. Here we report a very facile and reproducible method for the synthesis of CSNs with a control of particle morphology, crystallinity and phase selectivity, and provide important insight into the effect of core@shell configuration on the photocatalytic and optical properties of SiO_2@TiO_2 CSNs. For this purpose, synthesis of highly dispersed anatase nanocrystals (~5 nm) of high surface area was carried out by supporting these nanocrystals on silica sub-micron spheres in the form of a porous shell of controlled thickness (10–30 nm). The amorphous TiO_2 shell was crystallized into anatase using a low temperature (105 °C) hydrothermal treatment. The resulting CSNs were characterized by scanning electron microscopy, transmission electron microscopy, energy dispersive spectroscopy, x-ray photoelectron spectroscopy, X-ray diffraction, vibrational spectroscopy, zeta-potential measurements, BET surface area and electron paramagnetic resonance measurements. Both experimental data and theoretical simulations showed that due to the size of the complete particle (SiO_2@TiO_2), the general optical response of the system is regulated by Rayleigh scattering, exhibiting a red-shift of the extinction spectra as shell-thickness increases. The SiO_2@TiO_2 configuration leads to efficient light harvesting by increasing the optical path inside the core@shell particles. An enhanced photoactivity and good recyclability of SiO_2@TiO_2 CSNs was demonstrated compared to unsupported TiO_2. Together with BET surface area measurements, direct assessment of the density of photocatalytic sites probed by electron paramagnetic resonance measurements was used to provide insight into the enhanced photocatalytic activity of CSNs, which is also understood as a consequence of Rayleigh scattering, relative enhancement of the adsorption of organic molecules on the core@shell photocatalyst surface and increased optical path inside the SiO_2@TiO_2 particles. All these aspects are directly influenced by the core@shell configuration of SiO_2@TiO_2 samples.

1. Introduction

TiO_2 is still the most used among the photocatalysts based on benefit-cost ratio, as well as due to its suitable electronic and optical properties and good chemical stability. TiO_2 is widely used in photocatalysis [1,2], self-cleaning coatings [3], dye-sensitized solar

* Corresponding author. Tel.: +55 16 3373 9439.
E-mail address: uprf@iqsc.usp.br (U.P. Rodrigues-Filho).

http://dx.doi.org/10.1016/j.apcatb.2015.05.036
0926-3373/

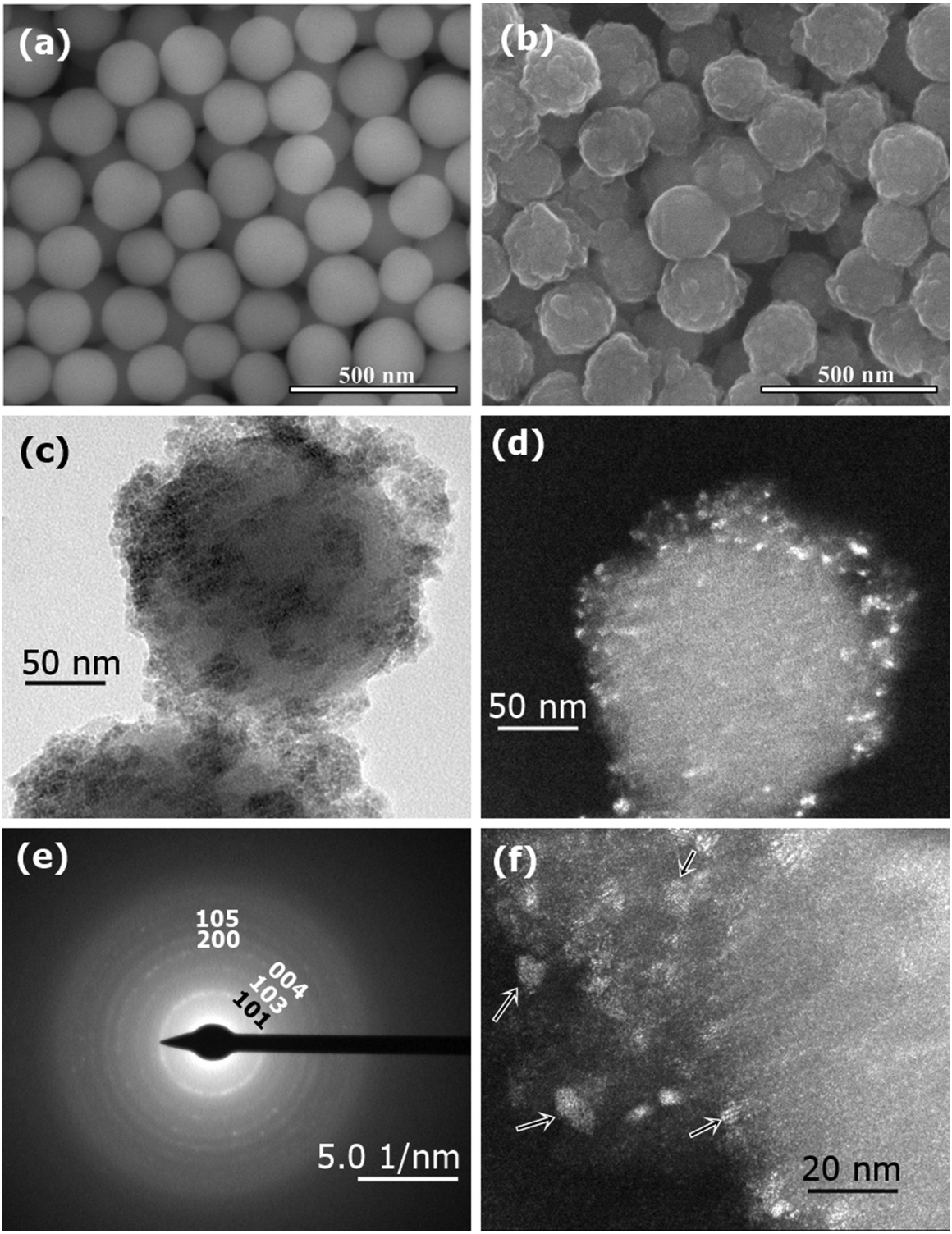

Fig. 1. FEG-SEM images of (a) unmodified silica and (b) CS-10; (c) bright field and (d) dark field TEM images of sample CS-20; (e) the SAED pattern and (f) the corresponding dark field image of CSNs obtained by collecting the electron diffracted from (1 0 1) and (1 0 3) planes of the SAED pattern.

cells [4], nanoparticles-coated facemasks [5], antibacterial coatings on medical devices [6] and optoelectronic and energy storage devices [7]. However, these applications, especially photocatalysis by TiO_2, closely depend on physical properties such as surface area, crystallinity, morphology, particle size and crystalline phase of titania, with anatase being the most active photocatalytic form of TiO_2 [8,9]. Despite such excellent properties of TiO_2, there are certain problems associated with nanometric TiO_2, which make practical applications difficult and costly. Such problems include nanoparticles' agglomeration [10], phase transformation [11,12], decrease in surface area upon thermal treatment [12,13], recombination of photogenerated electron–hole pair [14], lack of visible light photoactivity due to its wide band gap (E_g = 3.2 eV) [14] and the difficulty in recovery of the nanocatalyst from aqueous suspension.

To solve most of these problems, titania [15–20] and other functional metals/metal oxides [21,22] nanoparticles can be coated in

the form of a layer on the surface of thermally stable, low cost and high surface area core materials such as SiO_2, ZrO_2, MoO_3 and Fe_2O_3 [4,16]. Silica is one of the best core materials [23,24] for preparing the CSNs due to its rich and well-known surface chemistry and adsorption capacity [25], easy and controllable preparation by the Stöber method [26], optical transparency in the wavelength region where TiO_2 absorbs, low cost and high thermal and mechanical stability. Another advantage of using SiO_2 as the core material is that it can be easily leached out of the core@shell structure with an alkaline solution, for example, to obtain porous hollow spheres of the shell material with improved properties [19,20,22,27].

The core@shell configuration generally results in improved material properties [16,22] and the physical and chemical properties of CSNs can be tuned by controlling the morphology and thickness of the shell [18,19] or the size of the support material [17]. In most cases, the composite CSNs often show superior properties than either core or shell material alone [21,23]. For example, the SiO_2–TiO_2 heterogeneous system often exhibits better photocatalytic activity than TiO_2 alone [28–30], probably due to the fact that adsorption of organic compounds is improved [30] and aggregation of TiO_2 nanoparticles is minimized, thus leaving higher exposed surface area. Similarly, the anatase-to-rutile transformation is suppressed if TiO_2 is immobilized on silica [16,17] due to less inter-grain contact, knowing the fact that nucleation of rutile is triggered at the interface of two aggregated anatase particles [17].

Despite these unique features, the structure-properties relationship of CSNs are not yet fully understood, especially in connection to photocatalysis, as many parameters are simultaneously involved, such as the real surface area, electron–hole production efficiency upon photon absorption, recombination rate, and the photodegradation mechanism [31].

Here, we present a simple but efficient strategy for the preparation of SiO_2@TiO_2 hybrid particles with a fine control of crystallinity, phase selectivity, shell thickness and morphology. Compared to the unsupported TiO_2 nanoparticles of similar size, the SiO_2@TiO_2 CSNs exhibit better photocatalytic activity towards degradation of crystal violet (CV). The enhanced photocatalytic activity is analysed in terms of the structure of CSNs, the interfacial properties, the density of surface Ti(IV) sites able to support the formation of O_2^- radicals, as determined by EPR, and the optical response of CSNs.

2. Materials and methods

2.1. Reagents

Tetraethyl orthosilicate, TEOS, 98% and titanium (IV) isopropoxide, TiP, 97% and cellulose phosphate (fine mesh) were obtained from Sigma–Aldrich (USA). 2-propanol, with a water content of 0.04 % (as determined by Karl–Fisher titration using 870 KF titrino plus titrator, Metrohm, Switzerland) was from J.T. Backer (USA). Ammonium hydroxide, NH_4OH, 28%, and crystal violet, CV, 1%, were from QHEMIS (SP, Brazil). Stearic acid (SA) was obtained from Labsynth (SP, Brazil). All chemicals were used without further purification.

2.2. Synthesis of silica

The Stöber silica particles [26] of around (202 ± 20) nm in diameter were prepared by the hydrolysis of TEOS in basic media (pH ~ 11) at room temperature ($(25 \pm 2)^\circ$C) and a relative humidity of (65 ± 10)%. Briefly, 15 mL H_2O and 4 mL NH_4OH (28%) were added to 100 mL ethanol in a Teflon reactor and left under magnetic stirring for 20 min. Then, 3.0 mL of TEOS were quickly added to the above mixture, and left under constant magnetic stirring for 1 h. After this hydrolysis-polycondensation step, the mixture was neutralized with 5 mol L^{-1} HCl and centrifuged at 3500 rpm for 10 min. The supernatant was discarded and the precipitate was washed three times with water by suspending-centrifugation method. The resulting precipitate was dried at 70 °C for at least 15 h.

Table 1
Summary of the formulation parameters used for the synthesis of SiO_2@TiO_2 CSNs and the particle size distribution obtained from FEG-SEM analysis.

Sample	SiO_2 (g)	TiP (mmol)	(%)TiO_2 (wt.)	Particle size (nm)*
Silica	–	–	0	202 (20)
CS-10	0.2	0.46	10.4	225 (23)
CS-20	0.2	0.71	20.6	245 (25)
CS-30	0.2	1.4	31	250 (34)
CS-35	0.2	1.64	35	265 (33)
T1 (unsupported TiO_2)	–	1.64	100	6.7 (1.2)

* Particle size of composite SiO_2@TiO_2 particles except for T1. The values in bracket represent the standard deviation.

2.3. Synthesis of SiO_2@TiO_2 CSNs

Powder silica was dried at 110 °C for at least 1 h and 0.2 g of it was dispersed in 30 mL isopropanol by sonication for 1 h. This silica suspension was then transferred to a Teflon reactor and 50 mL more of isopropanol were added and left for 5 min under magnetic stirring. Then different amounts of titanium isopropoxide (TiP) (see Table 1) were quickly added and the reactor lid was tightly closed. The samples are labelled based on %TiO_2 (wt.%) they contain. The mixture was kept under magnetic stirring for 19 h. Then 9 mL water–alcohol mixture (3 mL H_2O:6 mL isopropanol) was slowly added (2 mL min^{-1}) and left for 1 h under magnetic stirring. The resulting colloidal suspension of SiO_2@TiO_2 was then centrifuged at 3500 rpm for 10 min, the supernatant was discarded and the precipitate was washed once with isopropanol and twice with deionized water. The amorphous titania shell was crystallized by hydrothermal treatment. The resulting amorphous CSNs were suspended in 50 mL H_2O and subjected to hydrothermal treatment at 105 °C for 24 h in a home made air-tight Teflon reactor (capacity 120 mL). The samples after hydrothermal treatment were centrifuged again at 3500 rpm for 10 min and the precipitated CSNs were dried at 100 °C under air. The unsupported TiO_2 (denoted as T1, hereafter) was also prepared using 500 μL (1.64 mmol) of TiP by the same procedure used for the preparation of CSNs but in the absence of SiO_2 in the reaction mixture. The particle size of anatase in T1 sample estimated from TEM images is comparable to that of CSNs (Supporting information, Fig. S1 and Table S1). The particle size of complete SiO_2@TiO_2 CSNs estimated from SEM images is also shown in Table 1.

2.4. Characterization techniques

FEG-SEM images of the samples coated with a thin carbon layer of about 5 nm were obtained using Inspect F-50 (FEI, Netherland) scanning electron microscope (SEM), equipped with an Everhart–Thornley SE detector, at an electron beam accelerating voltage of 15 kV. The average diameter of SiO_2 and CSNs was obtained by measuring the particles size from SEM images as given in Table 1. TEM analysis of the sample supported on carbon-coated copper grid (CFC-200Cu, EMS, USA) was done using an FEI TECNAI (G^2F20) transmission electron microscope operated at an accelerating voltage of 200 kV.

Raman spectra of SiO_2@TiO_2 CSNs powder were obtained with an LSI Dimension P-2 Raman spectrometer (Lambda solution, USA) equipped with 785 nm red laser and CCD detector.

X-ray diffractograms of powder samples of pure silica and CSNs were run at a scan rate of 0.5° min^{-1} with a Rigaku Rotaflex RU-200 X-ray diffractometer (Japan) operated at operated at 30 mA

and 40 kV using Ni-filtered Cu Kα X-ray radiation (λ = 1.540 Å). The anatase crystallite size was estimated using Scherrer equation [32] based on broadening of the diffraction peak at 2-theta value of 48° which correspond to the (2 0 0) plane of anatase.

The specific surface area (SSA) of the samples was estimated from nitrogen adsorption curves using the Brunaer–Emett–Teller (BET) method employing NOVA 1000 (Quantachrome, USA) surface area analyzer.

High resolution XPS spectra of SiO_2@TiO_2 sample deposited on carbon tape were obtained on a VSW HA-100 spherical analyzer employing AlKα radiation ($h\nu$ = 1486.6 eV) and using a constant analyzer pass energies of 22 eV, which produces a full width at half-maximum (FWHM) of 1.3 eV for the Au(4*f*7/2) line. The pressure during the measurements was always less than 2×10^{-8} mbar. Charge correction was made with respect to Si2*p* line at 103.5 eV [33].

The Zeta potential (ξ) of the samples was measured using a ZSNano Zetasizer instrument (ZEN 3600, Malvaran). The samples were dispersed in a 0.003 mol L^{-1} KCl solution to give a final concentration of 0.01%(w/v). The pH of the titration cell was varied by adding 0.01 mol L^{-1} HCl or KOH to the suspension. Since the isoelectric point (IEP) measured by electrophoretic mobility depends on the surface composition of the CSNs [34], the apparent surface coverage (ASC) can be calculated from the IEP data of the components by the equation [35,36]:

$$\mathrm{ASC} = \frac{M_{TiO_2}\left(IEP_{SiO_2} - IEP_{CSN}\right)}{\left[M_{SiO_2}\left(IEP_{CSN} - IEP_{TiO_2}\right) - M_{TiO_2}\left(IEP_{CSN} - IEP_{SiO_2}\right)\right]} \quad (1)$$

where M_{TiO_2} and M_{SiO_2} are the molecular weights of TiO_2 and SiO_2, respectively, and the subscripts CSN refer to the core@shell NPs.

2.5. Photocatalytic activity tests of CSNs

To evaluate the effect of shell structure and properties on photoactivity, 15 mg of CSNs or T1 were dispersed in 35 mL of deionized water by sonication for 30 min, and added to 35 mL of CV solution (20 ppm) in a cylindrical borosilicate vessel (internal diameter 4.5 cm). The system was kept under magnetic stirring under air during the experiment. After 30 min of magnetic stirring in dark, the samples were irradiated with a Lightningcure LC8 (Hamamatsu, Japan) Xe arc lamp equipped with a light guide placed at distance of 7 cm from the sample. The sample received 28.8 J cm^{-2} of UVA radiation per minute while UVB and UVC were filtered out by the borosilicate reactor. Aliquots before and after various irradiation intervals were collected in presence as well as in absence of CSNs (control experiment). After separation of the catalyst by centrifugation, the electronic spectra of the supernatant was collected and the area under CV peak (450–700 nm) was measured to evaluate the photocatalytic activity of the samples [37].

The photocatalytic activity of CSNs immobilized as thin films against an overlayer of stearic acid and CV was also proven for the design of self-cleaning surfaces (see supplementary section S1, Figs. S2–S4).

In order to investigate the recyclability and reuse of the CSNs, the photodegradation of CV with recycled and regenerated CSNs was tested. For this purpose, after the first photocatalytic test (cycle 1), the CSNs were recovered by centrifugation at 3500 rpm for 10 min, re-suspended in 35 mL of deionized water and then reused to photodegrade CV under the same conditions (cycle 2). The same procedure was repeated for cycle 2 through to cycle 4.

2.6. Adsorption experiments

Adsorption of CV on SiO_2@TiO_2 and unsupported TiO_2 (T1) was studied by adding 10 mL of 0.1% (w/v) suspension of T1 or CSNs to 40 mL of 5 ppm CV solution under constant magnetic stirring. The suspension was centrifuged after 5 min, 10 min, 30 min and 12 h of adsorption in dark and the electronic spectra of the supernatant solution was measured using Cary-50 (Varian, Australia) UV–vis spectrophotometer. The reference CV solution was prepared by mixing 40 mL of 5 ppm CV solution with 10 mL of distilled water. We observed no change in the spectra of the supernatant after 30 min, showing that the equilibrium is reached in 30 min (see Fig. S5).

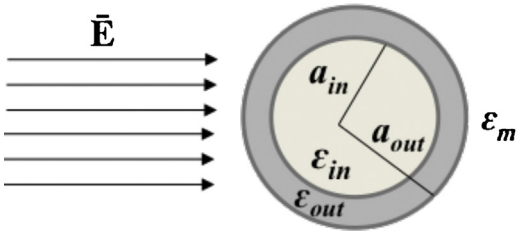

Scheme 1. Electric field $\vec{E}$ interacting with a core@shell particle; the core is determined by radius a_{in} and electrical permittivity ϵ_{in}, while shell is defined by radius a_{out} and electrical permittivity ϵ_{out}; ϵ_m represents the electrical permittivity of the surrounding media.

2.7. Electron paramagnetic resonance (EPR) measurements

EPR molecular probe analysis was carried out to find the relative number of Ti (IV) sites accessible to H_2O_2. For this purpose, 15 mg of the sample was placed in an EPR quartz tube (Wilmad Suprasil, OD 4 mm, wall thickness 0.8 mm) and 60 μL of 28% H_2O_2 (Synth, SP Brazil) was added to it, stirred for 2 min and the sample/H_2O_2 mixture left to react for 3 h. The EPR tube containing sample was placed in a cylindrical EPR cavity (ER 4103TM, Bruker) cooled to −196 °C using liquid N_2 and EPR spectrum recorded using a Bruker EMX Plus spectrometer operating at X-band frequencies and 100 KHz modulation frequency. For recording each spectrum, 8 scans were performed with a modulation amplitude set to 4G at a microwave power of 2 mW.

Double integration of the EPR signals was performed using WIN-EPR processing software (Bruker) to calculate the area of EPR peak. The spin density (spins.g^{-1}) of the samples was estimated by referencing the areas obtained to the *strong pitch* external standard from Bruker (product code 9510S180) which contains around 8.3×10^{15} spins per cm [38]. Though this value differs slightly among different reports, strong pitch can be used for the purpose of comparison among the different samples. Thus, the relative number of spins.g^{-1} of different samples was obtained by comparison with the number of spins.g^{-1} of *strong pitch* measured under the same conditions.

2.8. Optical properties of SiO_2@TiO_2

To study the optical response of the CSNs, a PerkinElmer LAMBDA 750 UV/Vis/NIR spectrophotometer equipped with a 60 mm integrating sphere was employed. The experimental data was fitted considering the extinction coefficient as a linear combination of absorption and Rayleigh scattering by the CSNs sample as the thickness of TiO_2 shell is increased. The model evaluates the extinction coefficient when an incident plane wave hits a core@shell (SiO_2@TiO_2) particle as shown in Scheme 1.

3. Results and discussion

3.1. Shell structure and morphology of the SiO_2@TiO_2

The properties of the nanocrystalline TiO_2 obtained by sol–gel method can be controlled by optimizing the process parameters [39]. The successful coating of all the TiO_2 generated by the hydrolysis-polycondensation step on the surface of SiO_2 obviously

depends on the balance between the rates of generation and deposition of TiO_2 NPs. To avoid the formation of coreless TiO_2 NPs, the precursor (TiP) was pre-adsorbed on the surface of SiO_2 for 19 h before the hydrolysis-condensation step. Hydrolysis of TiP possibly occurs during the adsorption step leading to the formation of interfacial Si—O—Ti bond between the partially hydrolysed precursor and silanol groups on the surface of silica. The formation of Si—O—Ti bond is confirmed by XPS analysis discussed later. The XRD analysis (Fig. S6) indicated that amorphous titania in CSNs was selectively crystalized into phase-pure anatase with good crystallinity (~95%) and small particle size (<10 nm) using the soft hydrothermal treatment (T = 105 °C, time = 24 h). The average anatase crystallite size determined from XRD (see later) and TEM analysis (Table S1) did not increase significantly with increasing the TiO_2 loading from 10 to 35%. The phase-selective formation of such small anatase nanocrystallite using a facile and reproducible method is one of the best features of the developed procedure.

The morphology and shell structure of the CSNs as function of TiP concentration was studied by FEG-SEM and TEM. The representative FEG-SEM images show that while pure SiO_2 has smooth spherical particles of around 200 nm (Fig. 1a), the surface of CSNs is rougher and decorated with small TiO_2 NPs (Fig. 1b and Fig. S7). For the highest amount of TiP added (CS-35 sample), the alkoxide precursor undergoes homogeneous nucleation, in addition to the deposition on the SiO_2 surface, leading to the formation of a mixture of CSNs and free or coreless TiO_2 nanoparticles (Fig. S7f). The average particle diameter exhibits an almost linear increment as function of TiO_2 loading (Fig. S8). Based on the particle size for pure silica and CSNs (Table 1), the measured shell-thickness was 11 nm, 21 nm, 24 nm and 31 nm for samples CS-10, CS-20, CS-30 and CS-35, respectively. However, the theoretical value of shell-thickness calculated for sample CS-30 considering spherical shape of CSNs is around 10 nm (see section S2 in ESI) which is about 2.5 times smaller than the measured thickness. This indicates that the titania shell in CSNs has a porous structure. Micro-EDS analysis also showed an almost linear increment in the bulk Ti/Si atomic ratio with the increase in theoretical Ti/Si ratio (Fig. S9), indicating that the deposition process of TiO_2 on silica is effective and reproducible.

The bright field TEM image of CS-20 shows the presence of titania nanocrystals around silica (Fig. 1c) which shine brightly when viewed in the dark field mode (Fig. 1d).

The EDS line-scan (Fig. S10) performed across the diameter of core@shell particles also confirms the formation of core@shell structure and suggests that the shell morphology changes from a "non-continuous" layer consisting of nano-island of TiO_2 to a relatively "continuous" one consisting of uniformly distributed and closely attached TiO_2 particles, though no complete layer is formed.

The selected area electron diffraction (SAED) pattern of the titania shell shown in Fig. 1e is typical of poly-nano-crystalline material [40]. The interplanar distances (±0.02 nm) obtained from SAED pattern are 0.374 nm, 0.259 nm, 0.219 nm, 0.187 nm and 0.164 nm which respectively correspond to (1 0 1), (1 0 3), (0 0 4), (2 0 0) and (1 0 5) crystal planes of the anatase (JCPDS# 21-1272) [41]. Raman spectra (Fig. S11) also confirmed the formation of phase pure anatase. The dark field TEM image obtained by collecting the electron diffracted from the (101) and (103) atomic planes clearly demonstrates the presence of titania nano-crystallites randomly distributed over the silica particles (Fig. 1f). The average crystallite size estimated from TEM images is around 6 ± 2 nm for all the CSNs (Table S1).

3.2. Interfacial properties

3.2.1. Specific surface area (SSA)

The SSA is one of the important parameters to be considered when analysing the interfacial properties and the photocatalytic activity. The SSA increases with the TiO_2 loading (Table 2). For instance, the SSA for SiO_2 particle is 33 $m^2 g^{-1}$ which increases to 126 $m^2 g^{-1}$ in case of sample CS-30. Such a significant increment in SSA indicates the formation of porous material. In fact, the nitrogen adsorption isotherm for CS-30 sample (Fig. S12) resembles that of type IV which is characteristic of mesoporous material [42]. The type of hysteresis observed approximates that of type II which characterizes solids with irregular, open or closed, cylindrical pores [42].

Table 2
Effect of TiO_2 loading on SSA, IEP and ASC of CSNs.

Sample	IEP (pH)	ASC (%)	SSA (±8) $m^2 g^{-1}$
SiO_2	2.59	–	33
CS-10	4.36	57	67
CS-20	4.99	74	92
CS-30	5.02	75	126
CS-35	5.08	76	105
T1	6.12	–	186

3.2.2. Measurement of isoelctric point (IEP) and apparent surface coverage (ASC)

Surface charge of the photocatalysts also plays an important role in the photocatalytic process. This parameter can be obtained from electrophoretic measurements at a given pH. The iso-electric point (IEP) defines the pH range for which the surface is positively or negatively charged. The surface charge affects both the adsorption process of organic molecules on photocatalysts surface and the driving force for migration of a hole at the surface. The latter competes with the electron-hole recombination; even for small TiO_2 particles, the band bending is negligible. Surface charge represents an average charge distribution at different surface sites–kinks, edges, planes–that are directly involved in the adsorption equilibrium constant [43].

The IEP and the corresponding apparent surface coverage, ASC, (the fraction of SiO_2 covered with TiO_2) [36] obtained from zeta potential (Fig. S13) through Eq. (1), are reported in Table 2. It can be seen that in a single coating step, the ASC reaches to around 75% for a TiO_2 loading greater than 10%, confirming the effectiveness of the coating procedure.

The IEP and hence the ASC remains almost constant for samples with more than 20% TiO_2 loading, thus further increase in TiO_2 loading simply results in stacking of anatase nanoparticles, which leads to the formation of a porous anatase shell (Scheme 2). Adsorption plays an important role in the overall reaction rate because: (i) once, the photolyte-surface distance is of the order of a covalent bond, direct hole transfer is favoured, (ii) it increases the probability of Langmuir Hinshelwood mechanism with adjacent -·OH (trapped holes) and (iii) it favours restructuring of the uncoordinated surface sites into their optimal octahedral structure, thus minimizing trapping of photogenerated electrons.

The porous structure of the shell and the effect of IEP is also evident from CV (a cationic dye) adsorption experiments shown in Fig. 2 where, for the same mass of solid photocatalysts, adsorption of CV on the CSNs (CS-30) is higher (~40% of initial concentration) than on unsupported TiO_2 (~3% only). This improved adsorption of CV on the CSNs plays important role in the photodegradation of these organic compounds [30,44–46] as discussed later.

3.2.3. FTIR and XPS analysis of the TiO_2/SiO_2 interface

FTIR and XPS analysis was performed to probe the bonding between TiO_2 and SiO_2 and check the purity of CSNs.

The FTIR spectra of uncoated SiO_2, pure TiO_2 and CSNs are compared in Fig. S14. The Ti—O—Si bond is generally regarded to absorb in the 910–960 cm^{-1} region [29,47]. However, due to the presence of silica bands at 949 cm^{-1} (Si—OH bonds) [48], the band in

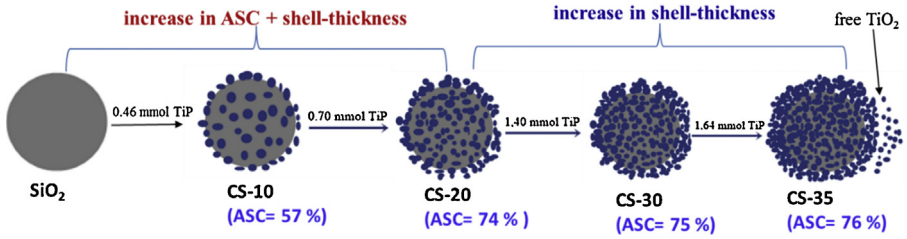

Scheme 2. Change in ASC and shell-thickness as function of amount of TiP used during the sol–gel synthesis of SiO_2@TiO_2 CSNs.

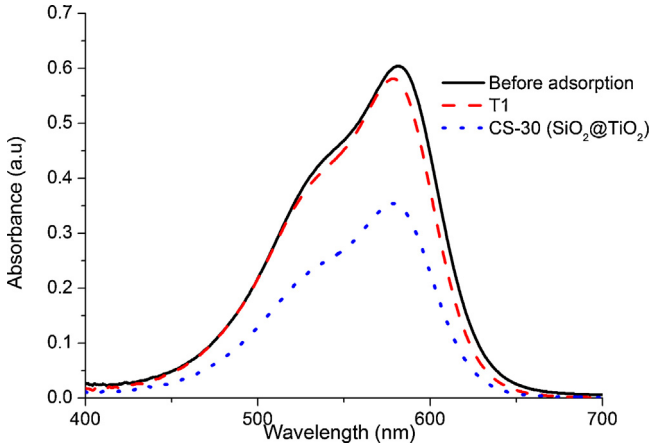

Fig. 2. Electronic absorption spectra of the supernatant of CV solution after 30 min adsorption on the T1 (dashed line) and CS-30 (dotted line).

910–960 cm^{-1} region (Ti—O—Si group) could not be observed in the FTIR spectra [29,47].

Also the FTIR spectra (Fig. S14) of CSNs showed no peak in the 2800–3000 cm^1 (C—H stretching region) indicating that the prepared CSNs are free from organic impurities, though no high temperature thermal treatment or calcination was used. This is remarkable for a synthetic route based on TiP that the hydrolysis of the TiP leads to formation of isopropanol, which is easily eliminated during the washing step and hydrothermal treatment.

XPS analysis was then performed to verify the formation of an interfacial Ti—O—Si bond between TiO_2 and SiO_2. The Si2*p* core region of SiO_2 can be fitted mainly as a single doublet (splitting = 0.61 eV) at binding energy (BE) of 103.5 eV corresponding to Si—O—Si bond [33] (Fig. 3a). Compared to the Si2*p* line of SiO_2 (FWHM = 2.04 eV), the Si2*p* line of CS-20 is broader (FWHM = 2.3 eV) and can be best fitted as two doublets (Fig. 3b). The extra component (peak-II) that occurs at 1.5 eV lower BE may be assigned to the Si—O—Ti bond. It turns out that a shift of electron density from Ti to Si atom through intermediate O atom leads to a decrease in BE of Si atom which confirms the formation of interfacial Ti—O—Si bond.

3.3. Density of surface reactive sites

The photocatalytic mechanism for TiO_2 needs surface active Ti species which we could probe by using molecular probes similar to the reactive oxygen radicals formed during photocatalysis. The reaction between H_2O_2 and SiO_2@TiO_2 CSNs can be taken as a model reaction to understand the photocatalytic behavior of CSNs which depends on the number of Ti(IV) sites accessible for surface reactions.

The EPR spectra of H_2O_2-treated samples shown in Fig. 4 are characterized by the spin-Hamiltonian parameters of g_{zz} = 2.025, g_{yy} = 2.009 and g_{xx} = 2.003 assigned to superoxide (O_2^-) radical anion adsorbed onto oxide surface [49]. EPR spectra are similar for all samples which indicates that the same superoxide radical anion

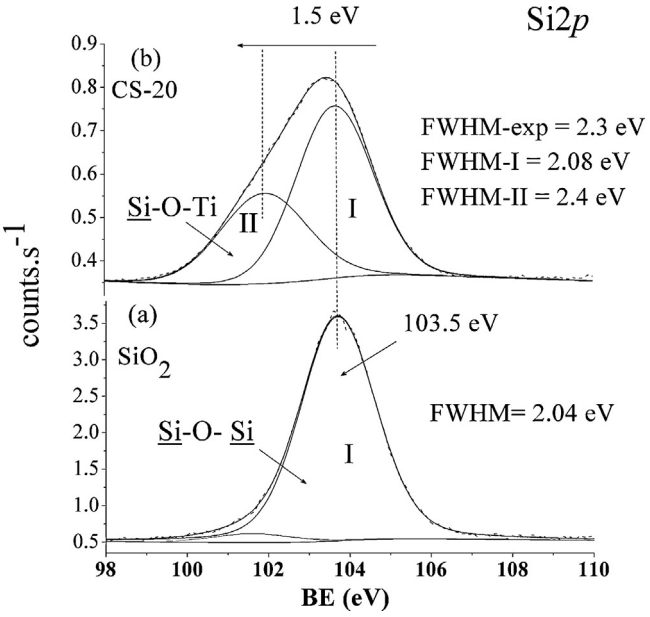

Fig. 3. Si2p XPS spectrum of (a) uncoated silica and (b) CS-20.

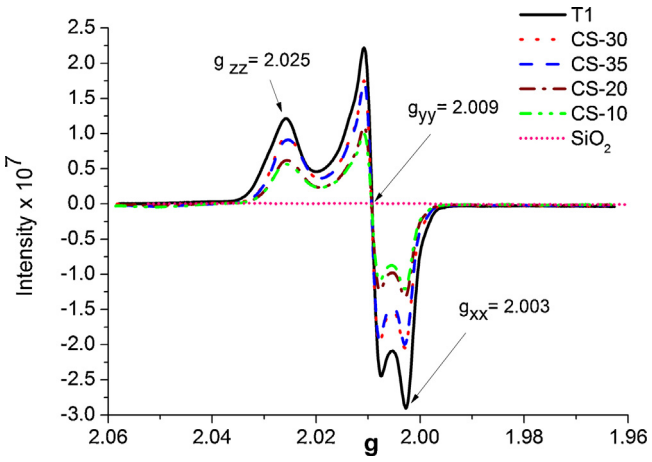

Fig. 4. EPR spectra of SiO_2, T1 and CSNs after 3 h reaction with 28% H_2O_2.

(O_2^-) is stabilized on similar Ti(IV) surface sites. No EPR signal was observed for uncoated SiO_2.

The estimated spin concentration for the sample derived from the EPR spectra is around $(4 \pm 1) \times 10^{17}$ spin.g^{-1}, which agrees well with the values reported in literature for the H_2O_2-treated TiO_2 [49]. It can be noted from Table 3 (middle column) that the spin density or the number of O_2^- radicals formed per gram of sample as a results of reaction with H_2O_2 increases slightly with the increase in SSA or shell-thickness.

Table 3
Density of surface spins for CSNs, TiO_2 and SiO_2.

Sample	10^{17} × spins g^{-1} sample	10^{18} × spins g^{-1} TiO_2
SiO_2	–	–
CS-10	3.0	2.1
CS-20	3.1	1.5
CS-30	4.8	1.6
CS-35	4.7	1.3
T1	6.6	0.6

Since the CSNs have different amount of TiO_2 (10–35%) and since only the TiO_2 component of CSNs (SiO_2@TiO_2) gives rise to the EPR signal, the number of spins.g^{-1} was normalized by the absolute amount of TiO_2 (rightmost column of Table 3). It can be noted from Table 3 that the TiO_2-normalized number of spins.g^{-1} is higher in SiO_2@TiO_2 samples ($1.6 \pm 0.3 \times 10^{18}$ spin.g^{-1} of TiO_2) compared to pure TiO_2 (0.6×10^{18} spins.g^{-1} of TiO_2). It turns out that the CSNs produce more superoxide radicals per g of TiO_2 than unsupported TiO_2 due to a higher exposure of Ti(IV) sites to H_2O_2 favoured by the de-aggregated, porous and permeable TiO_2 shell in CSNs. Thus CSNs are expected to have higher photoactivity as compared to pure TiO_2.

3.4. Optical properties of SiO_2@TiO_2 CSNs

The experimental UV–vis extinction spectra for the CSNs shown in Fig. 5 exhibit a red-shift (denoted by a green arrow) as shell-thickness is increased. The origin of this shift can be assigned to (i) an increase of scattering due to SiO_2@TiO_2 sub-micron particles with a porous shell and (ii) an increase of TiO_2 nanoparticles diameter. The hypothesis (i) was tested by simulating the extinction coefficient,Ext(λ),as a linear combination of the absorbance and the scattering terms:

$$\mathrm{Ext}(\lambda) = L \times C_{\mathrm{abs}}(\lambda) + N \times C_{\mathrm{sca}}(\lambda) \quad (2)$$

where L and N are proportionality constants which depend on the total number of dispersion centers, layer thickness, among other factors. The term $C_{\mathrm{abs}}(\lambda)$ corresponds to the absorption cross section, which can be well described for interband indirect transitions near the band-gap as:

$$C_{\mathrm{abs}}(\lambda) = \frac{(h\upsilon - E_g)^2}{h\upsilon} \quad (3)$$

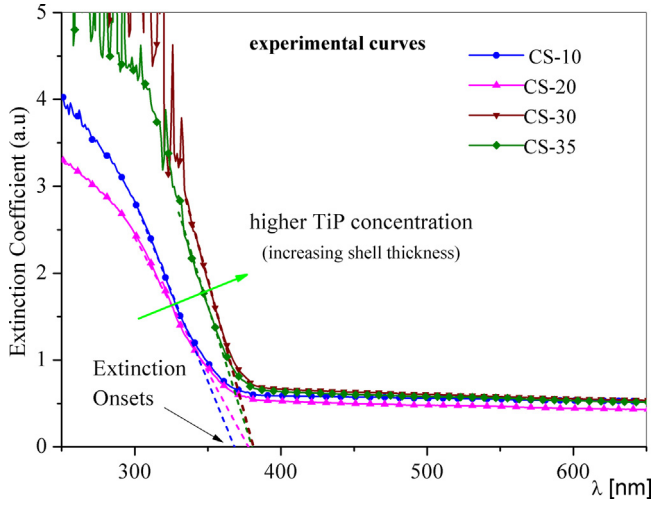

Fig. 5. Experimental extinction coefficient curves for the four samples under study; dashed lines denote the linear tendency that defines each extinction onset.

Table 4
Anatase crystallite size (XRD) and optical properties of SiO_2@TiO_2.

Sample	Crystallite size (nm) ±0.3 nm	Extinction onset (nm) ±10 nm
CS-10	4.4	368
CS-20	4.5	377
CS-30	4.3	380
CS-35	4.6	381
P25	21	394

where $h\upsilon$ is the photon energy and E_g is the optical gap energy, in this case for TiO_2 nanocrystallites. As regards the scattering term, $C_{\mathrm{sca}}(\lambda) = \frac{k^4}{6\pi}|\alpha^2|$ represents the Rayleigh scattering cross section coefficient, where k is the module of the surrounding medium wavevector [50] and α is the polarizability, which for core@shell particles, is given by [50]:

$$\alpha = 4\pi a_{\mathrm{out}}^3 \frac{(\epsilon_{\mathrm{out}} - \epsilon_{\mathrm{m}})(\epsilon_{\mathrm{in}} + 2\epsilon_{\mathrm{out}}) + f(\epsilon_{\mathrm{in}} - \epsilon_{\mathrm{out}})(\epsilon_{\mathrm{m}} + 2\epsilon_{\mathrm{out}})}{(\epsilon_{\mathrm{out}} + 2\epsilon_{\mathrm{m}})(\epsilon_{\mathrm{in}} - 2\epsilon_{\mathrm{out}}) + (2\epsilon_{\mathrm{out}} - \epsilon_{\mathrm{in}})(\epsilon_{\mathrm{in}} - \epsilon_{\mathrm{out}})} \quad (4)$$

Here $f = \frac{a_{\mathrm{in}}^3}{a_{\mathrm{out}}^3}$ represents the volume relation between core and shell. The geometric parameters a_{in} and a_{out} correspond to the inner and outer radius of the core@shell particle as denoted in Scheme 1. The constitutive relations ϵ_{in} and ϵ_{out} are the electrical permittivities of the core and shell, respectively. These constitutive parameters associate with the refractive index of each material by the relation $n = \sqrt{\epsilon}$for non-magnetic materials as the ones studied in this work. To represent the SiO_2 refractive index, a Cauchy [51] model was employed, while for the TiO_2 layers, a Lorentz-Cauchy [52] law was used which also took into consideration the mesoporosity of the shell.

The band gap energy (E_g) is an important factor directly associated with the wavelength range in which the semiconductor particles absorb light due to interband transition. The value of E_g can be altered by changing the particle size due to quantum size (Q-size) effect, as well as by the delocalization of molecular orbitals, which in turn creates energy traps and surface states on the band edge [53–55]. The absorbance term (Eq. (3)) mainly changes when the E_g value varies due to a change in the semiconductor nanocrystallite size.

Both TEM (Table S1) and XRD analysis (Table 4) confirmed the formation of anatase nanocrystallites of around 5 nm in all CSNs samples, independently of the TiP concentration. The invariance of the nanocrystallite size leads us to believe that the $C_{\mathrm{abs}}(\lambda)$ term should be the same among the different CSNs. The extinction onsets are also in accordance with these results, since the extinction onsets values do not differ significantly among the CSNs samples (Table 4). As regards the scattering term, C_{sca}, the change in the whole particle size as a result of increment of the shell-thickness introduces modifications in the optical response. According to Eq. (4), the core/shell size ratio should modify the polarizability among the samples which directly affects the C_{sca}.

Simulated extinction curves (Fig. 6) were obtained considering the variable TiO_2 shell-thickness derived from SEM images (see Table 1), but maintaining the absorbance term invariant (E_g value fixed at 3.31 eV– value calculated from the extinction onset of Fig. 5). The simulated curves show the same tendency as the experimental curves (see Fig. 5), with a red-shift of the curves due to the Rayleigh scattering term when the shell-thickness increases.

Comparing Figs. 5 and 6, it is possible to note the measured extinction coefficients (Fig. 5) exhibit a slight swap between samples CS10–CS20 and between CS30–CS35 with respect to the general tendency shown in Fig. 6. Although the shell is mesoporous in all samples, it is not possible to assure that the effective refractive index (TiO_2 wall + air pores) of the TiO_2 layer (n_{eff}^{TiO2}) remains

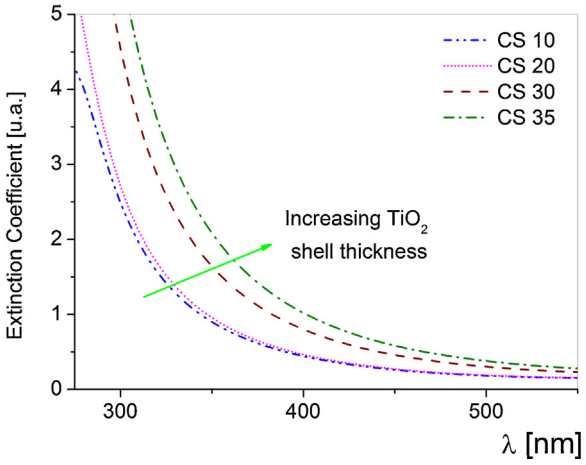

Fig. 6. Simulation curves for the extinction coefficients showing Rayleigh scattering is responsible for the red shift in the sample.

constant as the TiP concentration increases. Small variances in the n_{eff}^{TiO2} may be responsible for a swap in the extinction coefficient in Fig. 5.

To demonstrate this behaviour, extinction spectra of samples CS-30 and CS-35 were fitted considering slight differences in the parameters used in the Lorentz-Cauchy model which gave different n_{eff}^{TiO2} (eg., 2.38 and 2.00, respectively). The obtained results shown in Fig. 7a give a possible reason for the observed swap and are opposite to the general Rayleigh scattering tendency shown in Fig. 6.

To strengthen the idea that the $C_{abs}(\lambda)$ term does not produce a sensible variation in the optical response of the samples, the Q-size effect was evaluated considering different E_g values and a fixed size for a core@shell particle (CS-30). Simulated curves (Fig. 7b) for different E_g values ranging from 3.2 eV (the value for bulk anatase) up to 3.7 eV (which is the highest value of E_g obtained from the Tauc plots analysis, Fig S15) exhibit almost no differences. This result confirms that for the CSNs under study, the contribution of Q-size effect is less important as compared to the scattering effect. Moreover, the dashed red line in Fig. 7b shows that Q-size effect would be representative in some way for an imposed value of $E_g = 2$, which has no physical sense for the system under study.

The optical responses studied show that the extinction spectra of the samples analysed are mainly regulated by scattering phenomena which is responsible for the red-shift of the spectra.

3.5. Photocatalytic activity of CSNs

Fig. 8 displays a comparison of the photocatalytic activity of different CSNs as well as unsupported TiO_2 (T1) for the degradation of CV in suspension. The direct photolysis in the absence of any photocatalyst is very small under the experimental conditions since the borosilicate wall of the reactor filters out the more energetic UV-C wavelengths. It can be noted from Fig. 8 that the photoactivity of the samples follows the order: CS-30 > CS-35 > CS-20 > CS-10 > T1. It means that the CSNs photocatalysts, especially the ones with the maximum TiO_2 coverage of the silica surface (CS-30 and CS-35), exhibit higher photoactivity than pure TiO_2.

The fact that CSNs exhibit higher photoactivity than pure TiO_2 (T1) can be more clearly rationalized by considering that the CSNs sample contain only 10–35% TiO_2 (the active component) compared to T1 (100% TiO_2). For example, sample CS-10 and CS-20 with only 10% and 20% TiO_2 loading, respectively, still show

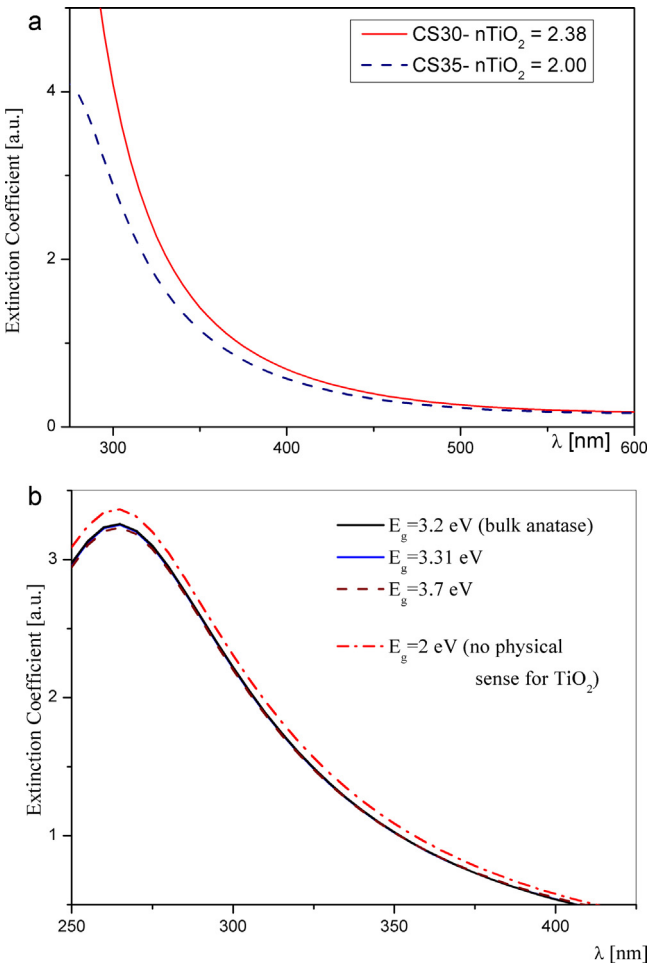

Fig. 7. Simulated extinction coefficients for: (a) different mesoporous TiO_2 refractive indexes, which might be responsible for the swap in the experimental curves, and (b) a fixed size of the core@shell (CS-35) using different values for E_g.

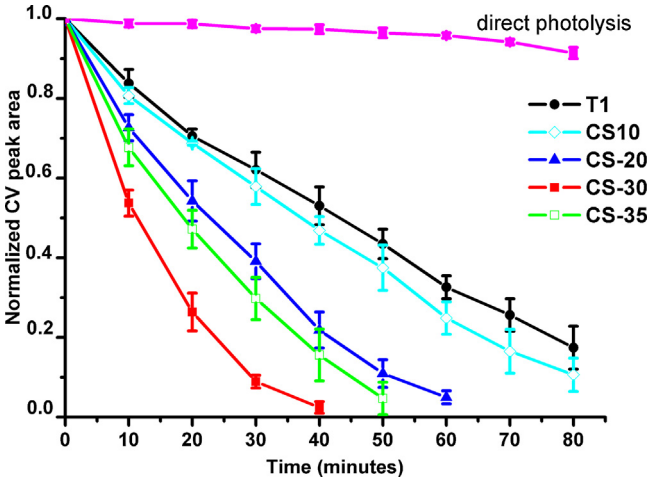

Fig. 8. Decrease in area of absorption band (430–700 nm) of CV as function of UV-irradiation in suspensions of different CSNs and T1 sample.

photoactivity better than T1 (100% TiO_2). Among the CSNs sample, the photoactivity increases with increase in TiO_2 loading or shell-thickness up to around 24 nm (CS-30). This increase in photoactivity of CSNs with increase in shell-thickness also points towards the accessibility of all the deposited titania NPs for photocatalytic reaction due to the porous nature of the shell and/or

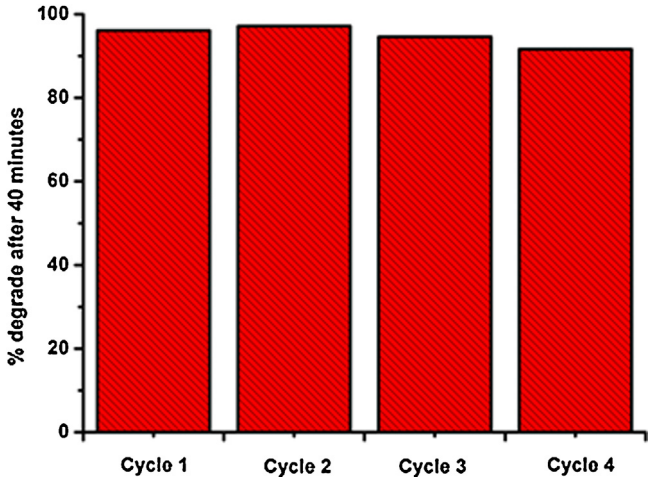

Fig. 9. Photodegradation of CV by the recycled CS-30 photocatalyst during repeated photocatalytic cycles showing the recyclable nature of CSNs photocatalyst.

better dispersion of TiO_2 particles on the surface of SiO_2. In case of dense TiO_2 shells, the photoactivity of the CSNs has been found to decrease with increase in shell-thickness [56].

The photoactivity of CS-35 is slightly lower than CS-30, though the former has higher content of TiO_2 (35%). Once homogeneous nucleation occurs in CS-35, it leads to the formation of free coreless TiO_2 nanoparticles (Fig. S7f) thus inducing the subsequent aggregation of these TiO_2 NPs. This in turn may lead to losses in SSA (Table 2) and photocatalytic activity

The photocatalytic activity of CSNs immobilized as thin films against an overlayer of stearic acid and crystal violet (CV) was also proven for the design of self-cleaning surfaces (Section S1, Supplementary information).

One of the important practical aspects of heterogeneous photocatalysis is the recovery of the used nanocatalyst from suspension and its reuse for several times in repeated photocatalytic cycles [57]. The recovery of the nanocatalyst (such as anatase) from aqueous suspension becomes easy when such small particles are supported on relatively large size support particles (such as SiO_2).

Fig. 9 shows the results of the recycling experiments where the same photocatalyst powder was repeatedly used for up to four times for the photodegradation of CV. The CSNs catalyst from first cycle was recovered by centrifugation and reused for the second cycles and so on. Fig. 9 clearly shows that the recycled CSNs do not lose their photocatalytic activity upon reuse for up to four times and more than 95% of CV is degraded in 40 min during each run. The CSNs thus offer the advantages of easy recovery by centrifugation and good recyclability due to persistence photoactivity of the recycled photocatalyst.

The better photocatalytic activity of CSNs as compared to T1 is explained in terms of the surface properties (number of active sites, SSA, IEP) and the optical properties of the system as discussed below

3.6. Why TiO_2@ SiO_2 CSNs are effective photocatalysts?

From the results of experiments and modelling presented in the preceding sections, it turns out that there are many factors contributing to the enhanced photocatalytic activity of CSNs compared to pure TiO_2 (T1) with the same crystallinity and particle size.

Better Dispersion of supported titania and improved adsorption of CV: The anatase particle size for all CSNs and T1 sample is almost the same; this parameter, therefore, has little impact on the observed order of photoactivity. However, an important difference between T1 and CSNs samples may be the degree of dispersion of anatase nanoparticles in suspension. While free TiO_2 might easily form aggregates in aqueous dispersions [58], better dispersion is expected in case of silica-supported titania [17,59]. For the supported nanoparticles covalently attached to the silica surface, aggregation is hindered giving higher accessibility to adsorbates (CV in this case). The resulting material allows improved adsorption (see Fig. 2) that facilitates the attack by either free or trapped holes [44–46]. In fact, when the photocatalyst is a mixture of CSNs and free TiO_2 nanoparticles (CS-35), the lower photocatalytic activity can be easily explained by losses of accessibility of TiO_2 nanoparticles due to homogeneous nucleation and possible aggregation.

Density of active Ti(IV) site: As discussed in Section 3.3, an estimation of the amount of O_2^- radical (per unit mass of TiO_2) produced by reaction of supported and unsupported TiO_2 with H_2O_2 (column 3 of Table 3) suggests that the Ti(IV) sites able to support the formation of Ti-OO(−) or Ti(OOH) surface complexes [49] are more accessible when TiO_2 nanoparticles are stacked on the SiO_2 surface. The observed order of photoactivity among the CSNs sample (CS-30 > CS-35 > CS-20 > CS-10) shown in Fig. 8 can be roughly explained by the EPR results which show that the number of active Ti(IV) sites on samples' surface increases with increase in SSA or TiO_2 loading (Table 3).

The EPR results, however, suggest that T1 should have higher photoactivity than all the CSNs under the experimental conditions due to the presence of higher number of active sites (6.6×10^{17} spins.g^{-1} sample) compared to CSNs ($(4 \pm 1) \times 10^{17}$ spins.g^{-1} sample). The fact that T1 has lower photoactivity than CSNs suggests that not only the total number of active sites but also the adsorption of organic compounds (CV in this case) on the photocatalyst surface (see Fig. 2) is necessary for the effective photodegradation of these organic compounds [14,30,44–46].

Optical Effects: The quasispherical shell of TiO_2 with mesoporous structure might generate a refraction index contrast among the different media (SiO_2, TiO_2 and air), leading to an increase of Rayleigh scattering, as the shell-thickness increases. Supported TiO_2 may act as a waveguide leading to multiple internal reflections inside the shell, which in turn might lead to an optimized light interaction with the semiconductor due to an increased optical path [4,60], thus enhancing the density of free and trapped holes at the surface. Such multiple reflections are more evident in case of relatively continuous shell (CS-30) and less important for discontinuous shell (CS-10).

Although the E_g remains unaltered due an invariance of the anatase crystallite size, the core@shell system fundamentally generates an optical confinement in the shell layer of the core@shell structure [4,60] and the degree of confinement is mainly influenced by the refractive index contrast between core and shell and between the shell and dielectric surrounding medium (see Eq. (4)). In particular, this interpretation provides insight in the better photocatalysis manifested by CS-30 compared towards CS-35 (Fig. 8). As proposed in Fig. 7a, the shell refractive index is higher for CS-30 than for CS-35 and this might cause more confinement inside the shell of CS-30 and an increased photoactivity of this sample, in addition to higher surface area of CS-30. Similarly, the slightly lower photoactivity of CS-10 compared to other CSNs may be related to the lack of complete surface coverage necessary for confining light inside the core@shell particle.

In summary, the enhanced photo-activity of CSNs compared to pristine TiO_2 (T1) may thus be attributed to a combined effect of the formation of porous shell of small particles (~5 nm) of anatase with high density of accessible Ti(IV) sites of appropriate surface coordination, better dispersion of supported TiO_2, good adsorption of organic molecules on CSNs and an increased light path due efficient photon harvesting by CSNs.

4. Conclusion

Stöber silica was effectively and reproducibly coated with a porous anatase layer of different thickness (10–30 nm) by simply varying the quantity of titanium isopropoxide (TiP), the TiO_2 precursor used. The pre-adsorption of the precursor (TiP) on the silica seems to be the key step for achieving higher TiO_2 loading (30%) and high apparent surface coverage (75%) in a single coating step without phase segregation. The linear relationships between theoretical and experimental Ti/Si ratios confirmed the effectiveness of the deposition process. The low temperature (105 °C) hydrothermal treatment was sufficient to obtain good crystallinity of the anatase shell. We clearly demonstrate that the optical response of SiO_2@TiO_2 CSNs is mainly influenced by Rayleigh scattering. Both our experimental and theoretical results show that the extinction onset does not vary (no E_g blue shift) and the extinction coefficient shows a red-shift due to Rayleigh scattering as the thickness of TiO_2 shell increases. Our results discussed above also suggest that the use of Tauc plot for determination of the optical gap energy (E_g) of TiO_2, especially in SiO_2@TiO_2 sample, without considering Rayleigh scattering can be misleading as the optical response of these hybrid CSNs is dominated by Rayleigh scattering. Owing to the porous nature of the shell, the increase in Ti/Si ratio or shell-thickness is accompanied by an increase in surface area and number of active Ti(IV) sites (probed by EPR spectroscopy) relevant for photocatalysis. The CSNs thus exhibit better photocatalytic activity than pure TiO_2, which is attributed to a combine effect of the formation of porous shell of small particles (~5 nm) of anatase, better dispersion of silica-supported anatase nanoparticles, improved adsorption of CV on the CSNs near the active sites and an increased light path and efficient light harvesting ability of CSNs. The CSNs immobilized as thin films exhibit good self-cleaning activity towards both saturated and unsaturated organic molecules. The method reported here thus allows a control of the TiO_2 loading and shell-thickness by simply varying the amount of precursor (TiP) which in turn provides a way to exploit the optical and photocatalytic properties of anatase NPs.

Author contributions

The manuscript was written through contributions of all authors. All authors have given approval to the final version of the manuscript.

Funding sources

The research was developed under the research grants # 2011/08120-0 and # 2013/24948-3 from São Paulo Research Foundation (FAPESP) and grant 308,653/2010-6 from the National Council for Scientific and Technological Development (CNPq). A. Bilmes and M.L. Martínez Ricci acknowledge financial support from Agencia Nacional de Promoción Científica y Tecnológica, ANPCYT-PICT-2010-0985/PICT2012-1167. We also acknowledge financial support from nBioNet Nanobiotechnology Network funded by Coordination of Improvement of Higher Education Personnel (CAPES, Brazil)).

Acknowledgment

Sajjad Ullah thanks The World Academy of Science (TWAS, Italy) and National Council for Scientific and Technological development (CNPq, Brazil) for PhD fellowship. Elias P. Ferreira-Neto thanks FAPESP for PhD fellowship (grant # 2013/24948-3). The authors wish to thank the Heterogeneous Catalysis and Electrochemistry Group at the Institute of Chemistry of São Carlos (IQSC), University of São Paulo (USP) for assistance in surface area measurements, Prof. Miguel Jafelicci Júnior and Wesley Renato Viali for assistance in the zeta potential measurements, Prof. Douglas Wagner Franco and Thiago Abrahão Silva for help in EPR measurements.

Appendix A. Supplementary data

Supplementary data associated with this article can be found, in the online version, at http://dx.doi.org/10.1016/j.apcatb.2015.05.036

References

[1] A.L. Linsebigler, G. Lu, J.T. Yates Jr., J.T. Yates, Photocatalysis on TiO2 Surfaces: principles, mechanisms, and selected results, Chem. Rev. 95 (1995) 5–758, http://dx.doi.org/10.1021/cr00035a013
[2] A. Fujishima, X. Zhang, D. Tryk, TiO_2 photocatalysis and related surface phenomena, Surf. Sci. Rep. 63 (2008) 515–582, http://dx.doi.org/10.1016/j.surfrep.2008.10.001
[3] E. Pakdel, W.a. Daoud, Self-cleaning cotton functionalized with TiO_2/SiO_2: focus on the role of silica, J. Colloid Interface Sci. 401 (2013) 1–7, http://dx.doi.org/10.1016/j.jcis.2013.03.016
[4] S. Son, S.H. Hwang, C. Kim, J.Y. Yun, J. Jang, Designed synthesis of SiO_2/TiO_2 core/shell structure as light scattering material for highly efficient dye-sensitized solar cells, ACS Appl. Mater. Interfaces 5 (2013) 4815–4820, http://dx.doi.org/10.1021/am400441v
[5] Y. Li, P. Leung, L. Yao, Q.W. Song, E. Newton, Antimicrobial effect of surgical masks coated with nanoparticles, J. Hosp. Infect. 62 (2006) 58–63, http://dx.doi.org/10.1016/j.jhin.2005.04.015
[6] D.W. Sheel, P. Evans, Photoactive and antibacterial TiO_2 thin films on stainless steel, Surf. Coatings Technol. 201 (2007) 9319–9324, http://dx.doi.org/10.1016/j.surfcoat.2007.04.013
[7] K. Saravanan, K. Ananthanarayanan, P. Balaya, Mesoporous TiO_2 with high packing density for superior lithium storage, Energy Environ. Sci. 3 (2010), http://dx.doi.org/10.1039/c003630g
[8] S. Banerjee, J. Gopal, P. Muraleedharan, A. Tyagi, B. Raj, Physics and chemistry of photocatalytic titanium dioxide: visualization of bactericidal activity using atomic force microscopy, Curr. Sci. 90 (2006) 1378–1383.
[9] J. Augustynski, The role of the surface intermediates in the photoelectrochemical behavior of anatase and rutile TiO_2, Electrochim. Acta 38 (1993) 43–46, http://dx.doi.org/10.1016/0013-4686(93) 80,008-n
[10] N. Mandzy, E. Grulke, T. Druffel, Breakage of TiO_2 agglomerates in electrostatically stabilized aqueous dispersions, Powder Technol. 160 (2005) 121–126, http://dx.doi.org/10.1016/j.powtec.2005.08.020
[11] D.A.H. Hanaor, M.H.N. Assadi, S. Li, A.B. Yu, C.C. Sorrell, Ab initio study of phase stability in doped TiO_2, Comput. Mech. 50 (2012) 185–194, http://dx.doi.org/10.1007/s00466-012-0728-4
[12] K. Raj, B. Viswanathan, Effect of surface area, pore volume and particle size of P25 titania on the phase transformation of anatase to rutile, Indian J. Chem. 48 (2009) 1378–1382.
[13] C.N. Satterfield, Heterogeneous Catalysis Industrial Practice, 2nd ed., McGraw-Hill, New York, 1991.
[14] J. Herrmann, Heterogeneous photocatalysis: fundamentals and applications to the removal of various types of aqueous pollutants, Catal. Today 53 (1999) 115–129, http://dx.doi.org/10.1016/S0920-5861(99)107-8
[15] A. Hanprasopwattana, S. Srinivasan, A.G. Sault, A.K. Datye, Titania coatings on monodisperse silica spheres (characterization using 2-propanol dehydration and TEM), Langmuir 12 (1996) 3173–3179, http://dx.doi.org/10.1021/la950808a
[16] A. Hanprasopwattana, T. Rieker, A. Sault, A. Datye, Morphology of titania coatings on silica gel, Catal. Lett. 45 (1997) 165–175.
[17] A. Li, Y. Jin, D. Muggli, D.T. Pierce, H. Aranwela, G.K. Marasinghe, et al., Nanoscale effects of silica particle supports on the formation and properties of TiO_2 nanocatalysts, Nanoscale 5 (2013) 5854–5862, http://dx.doi.org/10.1039/c3nr01287e
[18] T. Ohno, K. Numakura, H. Itoh, H. Suzuki, T. Matsuda, Control of the quantum size effect of TiO_2–SiO_2 hybrid particles, Mater. Lett. 63 (2009) 1737–1739, http://dx.doi.org/10.1016/j.matlet.2009.05.032
[19] J.B. Joo, I. Lee, M. Dahl, G.D. Moon, F. Zaera, Y. Yin, Controllable synthesis of mesoporous TiO_2 hollow shells: toward an efficient photocatalyst, Adv. Funct. Mater. 23 (2013) 4246–4254, http://dx.doi.org/10.1002/adfm.201300255
[20] J.B. Joo, Q. Zhang, I. Lee, M. Dahl, F. Zaera, Y. Yin, Mesoporous anatase titania hollow nanostructures though silica-protected calcination, Adv. Funct. Mater. 22 (2012) 166–174, http://dx.doi.org/10.1002/adfm.201101927
[21] S. Wei, Q. Wang, J. Zhu, L. Sun, H. Lin, Z. Guo, Multifunctional composite core–shell nanoparticles, Nanoscale 3 (2011) 4474, http://dx.doi.org/10.1039/c1nr1
[22] Q. Zhang, I. Lee, J.I.B. Joo, F. Zaera, Core–shell nanostructured catalysts, Acc. Chem. Res. 46 (2013) 1816–1824.
[23] W. Li, D. Zhao, Extension of the stöber method to construct mesoporous SiO_2 and TiO_2 shells for uniform multifunctional core–shell structures, Adv. Mater. 25 (2013) 142–149, http://dx.doi.org/10.1002/adma.201203547

[24] B.J. Jankiewicz, D. Jamiola, J. Choma, M. Jaroniec, Silica-metal core–shell nanostructures, Adv. Colloid Interface Sci. 170 (2012) 28–47, http://dx.doi.org/10.1016/j.cis.2011.11.002
[25] R.K. Iler, The Chemistry Of Silica, Wiley-Interscience, New York, 1978.
[26] A. Fink, W. Stöber, E. Bohn, Controlled growth of monodisperse silica spheres in the micron size range, J. Colloid Interface Sci. 26 (1968) 62–69, http://dx.doi.org/10.1016/0021-9797(68) 90,272-5
[27] J.B. Joo, Q. Zhang, M. Dahl, F. Zaera, Y. Yin, Synthesis, crystallinity control, and photocatalysis of nanostructured titanium dioxide shells, J. Mater. Res. 28 (2012) 2–368, http://dx.doi.org/10.1557/jmr.2012.280
[28] P. Periyat, K.V. Baiju, P. Mukundan, P.K. Pillai, K.G.K. Warrier, High temperature stable mesoporous anatase TiO_2 photocatalyst achieved by silica addition, Appl. Catal. A Gen. 349 (2008) 13–19, http://dx.doi.org/10.1016/j.apcata.2008.07.022
[29] S. Rasalingam, R. Peng, R.T. Koodali, Removal of hazardous pollutants from wastewaters: applications of TiO_2–SiO_2 mixed oxide materials, J. Nanomater. 42 (2014), http://dx.doi.org/10.1155/2014/617405
[30] C. Anderson, A.J. Bard, An improved photocatalyst of TiO_2/SiO_2 prepared by a Sol–gel synthesis, J. Phys. Chem. 99 (1995) 9882–9885, http://dx.doi.org/10.1021/j100024a033
[31] O. Carp, C.L. Huisman, A. Reller, Photoinduced reactivity of titanium dioxide, Prog. Solid State Chem. 32 (2004) 33–177, http://dx.doi.org/10.1016/j.progsolidstchem.2004.08.001
[32] A.R. West, Solid State Chemistry and its Applications, Wiley, Chichester [West Sussex] New York, 1984.
[33] T. Gross, M. Ramm, H. Sonntag, W. Unger, H.M. Weijers, E.H. Adem, An XPS analysis of different SiO_2 modifications employing a C 1s as well as an Au 4f7/2 static charge reference, Surf. Interface Anal. 18 (1992) 59–64, http://dx.doi.org/10.1002/sia.740180110
[34] G.A. Parks, The isoelectric points of solid oxides, solid hydroxides, and aqueous hydroxo complex systems, Chem. Rev. 65 (1965) 177–198, http://dx.doi.org/10.1021/cr60234a002
[35] P. Ruiz, B. Delmon, B. Koch, R. Castillo, Influence of preparation methods on the texture and structure of titania supported on silica, J. Mater. Chem. 4 (1994) 903–906, http://dx.doi.org/10.1039/jm9940400903
[36] F.J. Gil-Llambias, A.M. Escudey-Castro, Use of zero point charge measurements in determining the apparent surface coverage of molybdena in MoO_3/(-Al_2O_3 catalysts, J. Chem. Soc. Chem. Commun. 47 (1982) 8–479, http://dx.doi.org/10.1039/c39820000478
[37] S. Ullah, J.J.S. Acuña, A.A. Pasa, S.A. Bilmes, M.E. Vela, G. Benitez, et al., Photoactive layer-by-layer films of cellulose phosphate and titanium dioxide containing phosphotungstic acid, Appl. Surf. Sci. 277 (2013) 111–120, http://dx.doi.org/10.1016/j.apsusc.2013.04.011
[38] G. Ewing, Analytical Instrumentation Handbook, 3rd ed., Marcel Dekker, New York, 2005.
[39] J. Livage, M. Henry, C. Sanchez, Sol–gel chemistry of transition metal oxides, Prog. Solid State Chem. 18 (1988) 259–341.
[40] R.F. Egerton, Physical Principles of Electron Microscopy, Springer, US, Boston, MA, 2005, http://dx.doi.org/10.1007/b136495
[41] I. Djerdj, A.M. Tonejc, Structural investigations of nanocrystalline TiO_2 samples, J. Alloys Compd. 413 (2006) 159–174, http://dx.doi.org/10.1016/j.jallcom.2005.02.105
[42] G. Leofanti, M. Padovan, G. Tozzola, B. Venturelli, Surface area and pore texture of catalysts, Catal. Today 41 (1998) 207–219, http://dx.doi.org/10.1016/S0920-5861(98)00050-9
[43] A. Regazzoni, P. Mandelbaum, M. Matsuyoshi, S. Schiller, S.A. Bilmes, M. Blesa, Adsorption and photooxidation of salicylic acid on titanium dioxide: a surface complexation description, Langmuir 14 (1998) 868.
[44] C. Minero, F. Catozzo, E. Pelizzetti, Role of adsorption in photocatalyzed reactions of organic molecules in aqueous titania suspensions, Langmuir 8 (1992) 481–486.
[45] D.A. Friesen, L. Morello, J.V. Headley, C.H. Langford, Factors influencing relative efficiency in photo-oxidations of organic molecules by Cs3PW12O40 and TiO_2 colloidal photocatalysts, J. Photochem. Photobiol. A Chem. 133 (2000) 213–220, http://dx.doi.org/10.1016/S1010-6030(00) 237-9
[46] Y. Xu, C. Langford, UV-or visible-light-induced degradation of X3B on TiO_2 nanoparticles: the influence of adsorption, Langmuir 17 (2001) 897–902.
[47] X. Gao, I.E. Wachs, Titania–silica as catalysts: molecular structural characteristics and physico-chemical properties, Catal. Today 51 (1999) 233–254, http://dx.doi.org/10.1016/S0920-5861(99) 48-6
[48] A.N. Murashkevich, A.S. Lavitskaya, T.I. Barannikova, I.M. Zharskii, Infrared absorption spectra and structure of TiO_2–SiO_2 composites, J. Appl. Spectrosc. 75 (2008) 730–734, http://dx.doi.org/10.1007/s10812-008-9097-3
[49] K.L. Antcliff, D.M. Murphy, E. Griffiths, E. Giamello, The interaction of H_2O_2 with exchanged titanium oxide systems (TS-1, TiO_2, [Ti]-APO-5, Ti-ZSM-5), Phys, Chem. Chem. Phys. 5 (2003) 4306–4316, http://dx.doi.org/10.1039/b306398b
[50] C.F. Bohren, D.R. Huffman, Absorption and Scattering of Light by Small Particles, Wiley-VCH Verlag GmbH, Weinheim, Germany, 1998, http://dx.doi.org/10.1002/9783527618156
[51] H. Tompkins, W. McGahan, Spectroscopic Ellipsometry and Reflectometry: a User's Guide, Wiley-Interscience, New York, 1999.
[52] A.B. Djurisic, E.H. Li, Modeling the index of refraction of insulating solids with a modified lorentz oscillator model, Appl. Opt. 37 (1998) 5291–5297, http://dx.doi.org/10.1364/AO.37.005291
[53] L.E. Brus, A simple model for the ionization potential, electron affinity, and aqueous redox potentials of small semiconductor crystallites, J. Chem. Phys. 79 (1983), http://dx.doi.org/10.1063/1.445676
[54] M. Anpo, T. Shima, S. Kodama, Y. Kubokawa, Photocatalytic hydrogenation of CH_3CCH with H_2O on samll-particle TiO_2: size quantization and reaction intermediates, J. Phys. Chem. 91 (1987) 4305–4310, http://dx.doi.org/10.1021/j100300a021
[55] H. Lin, C. Huang, W. Li, C. Ni, S. Shah, Y. Tseng, Size dependency of nanocrystalline TiO_2 on its optical property and photocatalytic reactivity exemplified by 2-chlorophenol, Appl. Catal. B Environ. 68 (2006) 1–11, http://dx.doi.org/10.1016/j.apcatb.2006.07.018
[56] Z.-Y. Shen, L.-Y. Li, Y. Li, C.-C. Wang, Fabrication of hydroxyl group modified monodispersed hybrid silica particles and the h-SiO_2/TiO_2 core/shell microspheres as high performance photocatalyst for dye degradation, J. Colloid Interface Sci. 354 (2011) 196–201, http://dx.doi.org/10.1016/j.jcis.2010.10.023
[57] X. Li, X. Wu, G. He, J. Sun, W. Xiao, Y. Tan, Microspheroidization treatment of macroporous TiO_2 to enhance its recycling and prevent membrane fouling of photocatalysis – membrane system, Chem. Eng. J. 251 (2014) 58–68, http://dx.doi.org/10.1016/j.cej.2014.04.020
[58] Pagel, Dohtmann, Aggergation and deaggregation in TiO_2 (need be corrected), J. Phys. Chem. C 111 (2007) 4458–4464.
[59] M. Hirano, K. Ota, H. Iwata, Formation of anatase (TiO_2)/Silica (SiO_2) composite nanoparticles with high phase stability of 1300 °C from acidic solution by hydrolysis under hydrothermal condition, Chem. Mater. 16 (2004) 3725–3732.
[60] Y. Wang, E. Chen, H. Lai, B. Lu, Z. Hu, X. Qin, et al., Enhanced light scattering and photovoltaic performance for dye-sensitized solar cells by embedding submicron SiO_2/TiO_2 core/shell particles in photoanode, Ceram. Int. 39 (2013) 5407–5413, http://dx.doi.org/10.1016/j.ceramint.2012.12.048.